metals

MDPI

Article

Effect of Rolling Speed on Microstructural and Microtextural Evolution of Nb Tubes during Caliber-Rolling Process

Jongbeom Lee * and Haguk Jeong

Advanced Process and Materials R&D Group, Korea Institute of Industrial Technology, Incheon 21999, Korea; hgjeong@kitech.re.kr

* Correspondence: ljb01@kitech.re.kr; Tel.: +82-32-850-0378

Received: 9 April 2019; Accepted: 27 April 2019; Published: 29 April 2019

Abstract: This study investigated the fabrication of Nb tubes via the caliber-rolling process at various rolling speeds from 1.4 m/min to 9.9 m/min at ambient temperature, and the effect of the caliber-rolling speed on the microstructural and microtextural evolution of the Nb tubes. The caliber-rolling process affected the grain refinement when the Nb tube had a higher fraction of low angle grain boundaries. However, the grain size was identical regardless of the rolling speed. The dislocation density of the Nb tubes increased with the caliber-rolling speed according to the Orowan equation. The reduction of intensity for the <111> fiber texture and the development of the <112> fiber texture with the increase of the strain rate are considered to have decreased the internal energy by increasing the fraction of the low-energy Σ3 boundaries.

Keywords: Nb tube; caliber-rolling; grain boundaries; texture; electron backscatter diffraction

1. Introduction

Nb tubes are used in wires made of superconducting materials, such as NbTi, Nb_3Sn, Nb_3Al, and MgB_2/Nb/Cu, as a diffusion barrier for MgB_2/Nb/Cu, which disturbs the chemical reaction between the Mg-B powders and Cu, and as a superconductor for NbTi and Nb_3Sn, which have superconductive properties [1–4]. Superconductive wires are fabricated using the drawing process or caliber-rolling to reduce their diameter to less than 1 mm. To manufacture a superconductive wire without fracturing, it is very important to improve the ductility of the Nb tube such that it can play a role as a diffusion barrier or a superconductive material. This can be achieved by using optimal conditions in the deformation process. In previous work on the drawing process [5,6], it was stated that an electric field significantly affects the nature of grain boundaries via a localized Joule heating effect, which was experimentally proved by Zhan et al. [7]. The electrically assisted wire drawing process has also been proved to be a feasible technique that enhances the material formability compared to the conventional wire drawing process [8].

The caliber-rolling process is very simple compared with the drawing process, and the preparation time for the samples is short because additional processing, such as the swaging process so that samples can fit or enter into the die, is not required. Additionally, the caliber-rolling process can achieve a larger area of reduction compared with the drawing process. The deformation process is very suitable for making ultrafine grain microstructures, owing to its characteristic of large strain in multipass and multidirectional manufacturing [9]. The mode of deformation and related micromechanisms can be influenced by deformation factors, such as the deformation temperature, strain, and strain rate. Amongst the various factors, the caliber-rolling speed is closely related to productivity. Therefore, it is very important to investigate the microstructure and microtexture of Nb tubes during deformation so as to reduce fracturing. To date, the effect of the caliber-rolling speed, that is, the strain rate, on the microstructure and microtexture of the Nb tube has not been reported.

The deformation of body-centered cubic (bcc) crystal materials, such as Nb tubes, occurs mostly via slip. However, twins have also been observed at low temperatures and/or at high strain rates in certain orientations. The commonly active slip systems of bcc crystals are {110}<111> and {112}/<111>, but non-crystallographic slip planes have often been observed. Face centered-cubic (fcc) single crystals have consistent slip directions and dislocation glide planes governed by Schmid's law. Moreover, the plastic deformation of bcc single crystals is characterized by the inapplicability of Schmid's law and anomalies with regard to the prediction of operative slip systems [10,11].

In terms of the strain rate's influence on the dislocation mode and slip system, at very high strain rates, the stress can be sufficiently high to mechanically force the dislocation past all barriers without the aid of thermal fluctuations. Experimental data obtained from uniaxial tensile tests indicate that, in most metals, this occurs when the plastic shear strain rate reaches a value of approximately 5×10^3 s^{-1} [12]. However, such a high strain rate cannot be applied to the caliber-rolling process considered in this study.

This study investigated the effect of the caliber-rolling speed on the microstructural and microtextural evolution of Nb tubes during the caliber-rolling process. The objective of this investigation was to determine which dislocation mechanism contributes to the formation of the grain boundaries and to the misorientation between the grain boundaries, and how the dislocation density increases or decreases based on the electron backscatter diffraction (EBSD) data.

2. Materials and Methods

This study used Nb tubes with a purity of over 99.95% (Baoji Junuo Metal Materials Co., Ltd., Baoji, China) and an impurity content of approximately 50 ppm. The Nb tubes had a diameter of 20 mm and thickness of 1.5 mm. In preparation for the caliber-rolling process, the Nb tubes were cut to a length of 100 mm. The Nb tubes with an initial diameter of 20 mm and length of 100 mm were rolled with several reduction areas (RAs) per pass of 8–12%. The *RA* per pass was calculated using Equation (1):

$$RA = \frac{A_0 - A_f}{A_0} \times 100(\%) \quad (1)$$

where A_0 and A_f denote the initial and final cross-sectional areas, respectively. In this study, the total RA of six steps was approximately 48%. Figure 1a shows a schematic representation of the caliber-rolling and diameter in each step. The tests were carried out at a rolling speed of 1.4–9.9 m/min at ambient temperature. The caliber-rolling direction was kept constant at every rolling pass. The deformation strain rate was measured from the length of the Nb tube in the final step at the rolling speed of 1.4, 4.2, 7.1, and 9.9 m/min, and was 1, 3, 5, and 7 min^{-1}, respectively.

The grain orientation was determined using the electron back-scatter diffraction (EBSD) technique combined with high resolution thermal field emission scanning electron microscopy (FE-SEM; S-4300SE, Hitachi. Co., Ltd., Hitachi, Japan). Before and after each deformation, the EBSD maps were obtained in the longitudinal (RD/TD) section (Figure 1b) using step scans with steps of 1.2 μm. On one of the internal surfaces, the observation area was 500 μm × 500 μm. For the EBSD analysis of the samples, electro-polishing was used during the fine grinding process to ensure that the orientation remained unaffected by the treatment procedure. The image quality of the Kikuchi pattern at each EBSD data point was obtained using the OIM analysis software (OIM analysis V8, TSL Co., Ltd., Tokyo, Japan). A relatively clean image was obtained using the grain dilution clean-up function with a tolerance of 5°.

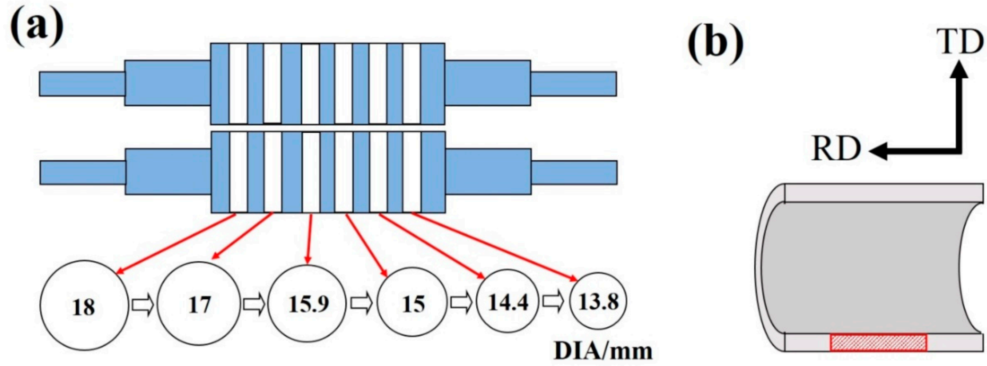

Figure 1. (**a**) Schematic representation of caliber-rolling process showing the diameter of each roller, and (**b**) the red diagonal area is the observed area for EBSD.

3. Results

Figure 2 shows the grain boundary maps obtained from the EBSD data for the Nb tube before and after the deformation at a caliber-rolling speed of 1.4–9.9 m/min at ambient temperature. The grain boundaries measured by the EBSD (Figure 2) were classified into both boundaries: low-angle boundary (LAB) and high-angle boundary (HAB). The red lines and the blue lines indicate the LABs and the HABs, respectively. Both boundaries can also be defined as follows. The LABs consist of low misoriented low-angle boundaries (LMLABs, 2–5°) and high misoriented low-angle boundaries (HMLABs, 5–15°). In a similar manner, the HABs consist of intermediate misoriented high-angle boundaries (IMHABs, 15–40°) and high misoriented high-angle boundaries (HMHABs > 40°) [13]. The LABs and HABs equivalently existed in the as-received Nb tubes. However, as shown in Figure 2b–e, the population of LABs largely increased after the Nb tubes were caliber-rolled at ambient temperature, regardless of the caliber-rolling speed. In the caliber-rolling process, the LABs had noticeable caliber-rolled samples inside the grains and near the grain boundaries of the Nb tube. Moreover, it is obvious that the low angle grain boundaries mainly formed in the microstructure of the caliber-rolled Nb tube by increasing the rolling speed at ambient temperature.

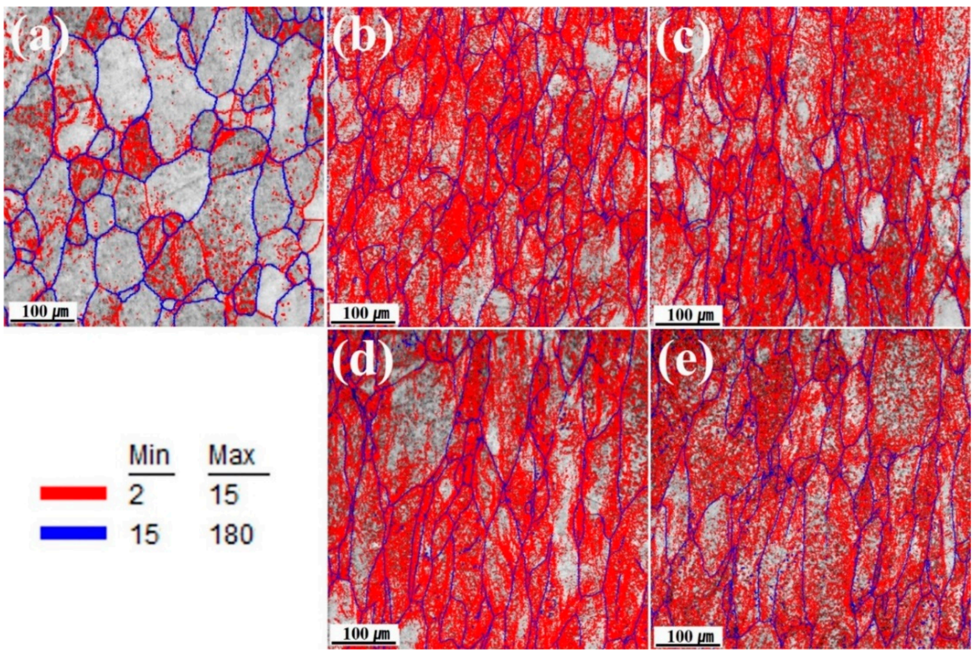

Figure 2. EBSD grain boundary maps of (**a**) as-received Nb tubes, and Nb tubes caliber-rolled at rolling-speeds of (**b**) 1.4 m/min, (**c**) 4.2 m/min, (**d**) 7.1 m/min, and (**e**) 9.9 m/min.

Figure 3a shows the fraction of the classified grain boundaries consisting of the Nb tube microstructure before and after the caliber-rolling process. Here, the fraction of each grain boundary was calculated to divide the length of the grain boundary by the length of total grain boundaries. As can be seen from the graph, the fraction of the LABs increased after the caliber-rolling process was applied. The mean value of the grain size was calculated from the EBSD data as shown in Figure 3b. The mean grain size of the as-received Nb tubes dramatically decreased during the caliber-rolling process; however, only a negligible difference of the mean grain size was observed as a function of the caliber-rolling speed in the samples, as shown in Figure 3b. As can be seen in Figure 2, the as-received Nb tubes consisted of equiaxed grains; however, the shape of the grains changed and became elongated by increasing the caliber-rolling speed. The grain shape aspect ratio was calculated from the EBSD data and plotted for all samples, as shown in Figure 3c. The images shown in Figure 2 were used to calculate the microstructure quantifiers, such as the grain shape aspect ratio, which is a dimensionless number representing the grain shape and its elongation, that is, the ratio of the lowest diameter to the largest diameter ($A_r = d_{min}/d_{max}$) within a grain. Hence, a grain with a lower grain shape aspect ratio will become more elongated than a grain with a higher grain shape aspect ratio. The graph shown in Figure 3c indicates that the grains gradually elongated as the A_r value decreased with the increase of the caliber-rolling speed.

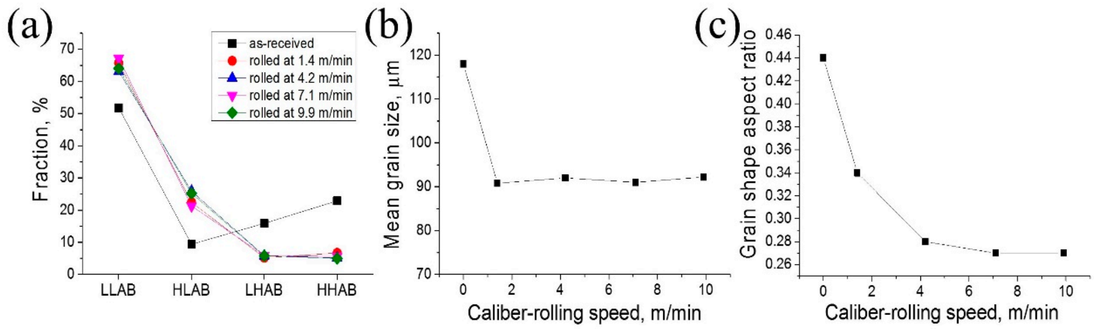

Figure 3. (**a**) Fraction of LABs and HABs versus caliber-rolling speeds, (**b**) variation of mean grain size, and (**c**) grain shape aspect ratio with caliber-rolling speed in Nb tubes.

Figure 4a–c shows the kernel average misorientation (KAM), distribution of the as-received Nb tubes, and caliber-rolled tubes at 1.4 and 9.9 mm/min, respectively, represented by color-coded maps. The KAM can evaluate the local strain distribution in each grain and is the most appropriate quantity for this purpose because its value reflects the stored strain energy [14,15]. The Nb samples subjected to the caliber-rolling process had larger orientated grains than the as-received Nb tubes. Additionally, it was observed that the local strains induced by the orientation gradient occurred closer to the grain boundaries rather than inside the grains. The Nb samples caliber-rolled at 1.4 m/min (Figure 4b) had larger orientation gradients in all grains, whereas the Nb samples subjected to the caliber-rolling process at 9.9 m/min had smaller orientation gradients. Therefore, the increase of the orientation gradients indicates that the dislocation density caused the local strains to increase when the caliber-rolling process was applied to the Nb tubes at lower speeds. The orientation gradients in the grain are attributed to the stored strain energy during the deformation. According to Figure 4a–c, the stored strain energy originated from the individual LMLABs or HMLABs. In turn, the stored strain energy increased with the increase of LABs by rotating the neighboring grains from 2° to 15°. From the EBSD data, it was found that the number of LABs in the as-received Nb tubes, Nb tubes caliber-rolled at 1.4 m/min, and Nb tubes caliber-rolled at 9.9 m/min, was 35,162, 158,218, and 146,025, respectively. This is attributed to the dislocation accumulation and multiplication caused by the local inhomogeneous deformation of an anisotropic plastic behavior [6]. According to the observations, the number of LABs in the Nb tubes increased with the increase of the caliber-rolling speed. The mean KAM value increased from 0.07 to 0.075 rad by increasing the caliber-rolling speed from 1.4 to 9.9 mm/min. This means that a lower local strain energy resulted in lower dislocation density. The dislocation density ρ can be calculated using the average misorientation measurement and dislocation boundary spacing as follows [14,16–18]:

$$\rho \approx \frac{\alpha\theta}{bd} \quad (2)$$

where θ is the average misorientation angle across the dislocation boundaries, b is the magnitude of the Burgers vector, d is the average spacing of all dislocation boundaries, and α is a constant.

The stored strain energy (E) per unit volume can be obtained as follows [17]:

$$E = \frac{1}{2}G\rho b^2 \quad (3)$$

where G is the shear modulus. According to Equation (3), the stored strain energy is proportional to the dislocation density; therefore, the grain orientation caused by the local strain is related to the dislocation density.

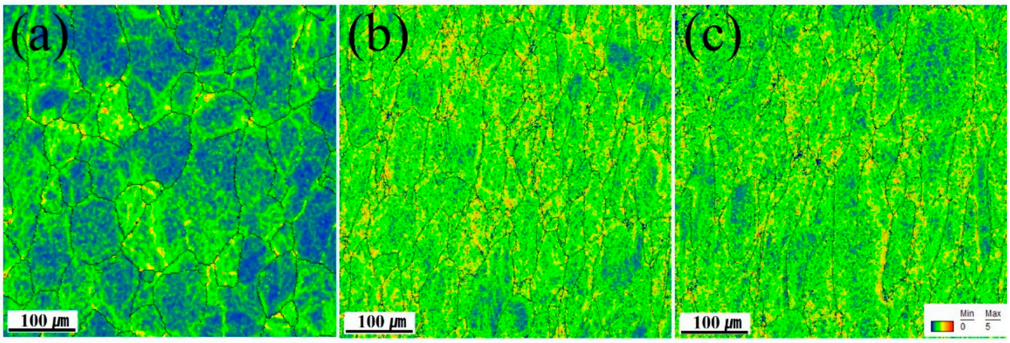

Figure 4. KAM maps of (**a**) as-received Nb tubes, and Nb tubes caliber-rolled at rolling speeds of (**b**) 1.4 m/min and (**c**) 9.9 m/min. The color code is consistent with the respective KAM value ranges shown at the bottom right.

Table 1 presents the dislocation density calculated from the KAM value using Equation (1). The KAM values were affected by the scan step size, which was constant at d = 1.2 μm. For pure niobium, α = 3 for boundaries with mixed characters, while b = 0.285 nm and θ is a radian value for the mean angle of the misoriented boundaries. The results presented in Table 1 indicate that the as-received Nb tube had the highest θ value and lowest ρ value. Moreover, based on Table 1, it was assumed that the ρ value increased as a function of the caliber-rolling speed in the Nb tube. Furthermore, the dislocation density was probably underestimated, owing to the existence of dislocations that did not contribute to the misorientation build-up [16].

Table 1. Dislocation density before and after Nb tube was caliber-rolled.

Samples	b (nm)	θ (rad)	d (μm)	Area (μm^2)	Density (10^{14} m^{-2})
As-received	0.285	0.046	1.2	250,000	1.95
1.4 m/min	0.285	0.07	1.2	250,000	2.47
4.2 m/min	0.285	0.071	1.2	250,000	2.49
7.1 m/min	0.285	0.073	1.2	250,000	2.59
9.9 m/min	0.285	0.075	1.2	250,000	2.64

In addition to the abovementioned microstructural evolution, the evolution of the texture during the caliber-rolling process was also investigated at a rolling speed from 0–9.9 m/min, as shown in Figure 5. The results suggest that the deformation textures of the caliber-rolled Nb tubes could be characterized as a major <111> fiber texture, except for the Nb tube caliber-rolled at 9.9 m/min. Moreover, the Nb tube caliber-rolled at the highest rolling speed had a major <112> fiber texture with low intensity and consisted of expanded texture components. It was also observed that, throughout the samples, the texture intensity for the caliber-rolled Nb tubes decreased with the increase of the caliber-rolling speed. In turn, the increase of the caliber-rolling speed resulted in the reduction of the intensity for the <111> texture component at the center areas of the Nb tube, which was related to the development of the slip system.

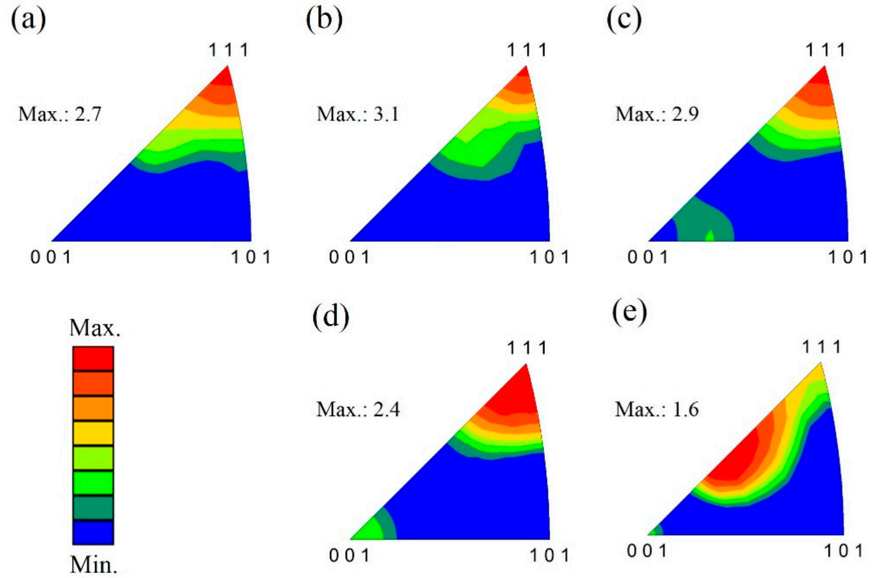

Figure 5. Texture evolution based on the inverse pole figure (IPF of) (**a**) as-received Nb tubes, and Nb tubes caliber-rolled at rolling speed of (**b**) 1.4 m/min, (**c**) 4.2 m/min, (**d**) 7.1 m/min, and (**e**) 9.9 m/min.

4. Discussion

In the microstructural evolution obtained from the EBSD data, it can be seen that the fraction of the LMLABs and HMLABs in the as-received Nb tubes significantly increased, while that of the LMHABs and HMHABs decreased during the caliber-rolling process. According to the results, the dynamic recovery and recrystallization did not occur in the samples, regardless of the rolling speed. Hence, it would be difficult for them to occur in the Nb tubes as a result of the caliber-rolling process at ambient temperature because, for Nb materials, recrystallization requires over 1/3 of the melting temperature (2750 K °C). Evidently, dynamic recrystallization did not occur during the caliber-rolling process at ambient temperature because the fraction of the LMHABs and HMHABs did not change with the increase of the caliber-rolling speed. Moreover, the microstructure of the Nb tubes was refined by the formation of the substructure or low angle boundaries, which led to the increase of the dislocation density during the caliber-rolling deformation, based on the results presented in Table 1. Based on the data pertaining to the reduction of the tube area and tube length after the caliber-rolling process, the caliber-speed could be transferred to the strain rate. The strain rate values were 0.017, 0.054, 0.087, and 0.12 s^{-1} for 1.4, 4.2, 7.1, and 9.9 mm/min, respectively. The relationship between the dislocation density and the strain rate can be expressed using the Orowan equation as follows [12,19]:

$$\dot{\varepsilon} \approx b\rho s$$

where s is the dislocation velocity. This equation is in good agreement with the values listed in Table 1. Because the degree of strain-rate increment was larger than that of the dislocation density compared with the strain rate and dislocation density in the samples, it was assumed that the occurrence of dislocation decreased as a function of the strain rate. This should be considered with regard to the factor of generated heat during the deformation, which increases the dislocation because the dislocations can move without pile-up and dislocation interactions as much as possible. Thus, the dislocation density must decrease. In this study, the generated heat increased with the increase of the caliber-rolling speed because the heat was induced by the friction between the Nb tubes and the caliber-roller during the caliber-rolling deformation. However, the heat was negligible because the difference of the strain rate between the highest value and the lowest value was less than 10-fold.

Another reason for the slow increase of the dislocation density with the caliber-rolling speed was the dislocation activity. The activation volume, that is, the dislocation activity, for the deformation of bcc metals was in the range of $5b^3$ (where b is Burgers vector), whereas the fcc activation volume was 10 to 100 times larger. Furthermore, the activation volume of the bcc metals was independent of the strain, while that for the fcc metals decreased as the strain increased [20]. Additionally, the analysis based on the combined operation of the Peierls mechanism and dislocation drag process appeared to be valid in the activation volume. In this study, the dislocation activity was attributed to the Peierls mechanism because, for strain rates below approximately 1000 s^{-1}, the contribution of the dislocation drag process was small [12].

In bcc metals, mechanical twinning is an important mode of deformation, particularly at low temperatures. The twins form on the {112} planes and have a resulting shear of $s = \frac{1}{\sqrt{2}}$ in the <111> direction. The existing models of twinning in bcc metals are based on a pole mechanism, which requires a relatively complex dislocation dissociation to form the spiraling partial dislocation responsible for the formation of the mechanical twin [21,22]. According to Figure 3, the decrease of intensity as a function of the caliber-rolling speed for the <111> pole figure in the samples may have been caused by the formation of the spiraling partial dislocation, which indicates the presence of a weak <001> pole figure in caliber-rolled samples over a speed of 4.2 m/min. Additionally, this shows that, if the mobile dislocation density is sufficiently large, then the strain can be accommodated by the dislocation motion. If the number of mobile dislocations is insufficient, another deformation mechanism, such as twinning, is necessary. This mechanism is consistent with the inverse pole figure (IPF) result shown in Figure 3.

The grain boundary map of the EBSD data can be used to calculate the misorientation axis when the misorientation angle has been determined. This means that the EBSD data can be used to identify specific boundaries defined not just by the misorientation angle, but also by a combination of the misorientation angle and the misorientation axis. Therefore, it is useful to identify the twin boundaries that are a subset of the coincident site lattice (CSL) boundaries, which are special boundaries that fulfil the coincident site lattice criteria whereby the lattices are sharing various lattice sites. Figure 6 shows the population of the CSL boundaries in the caliber-rolled samples at speeds ranging from 1.4 to 9.9 m/min. The fraction of the CSL boundaries was significantly low compared with that of the fcc materials [23]. However, the $\Sigma3$ boundary had a relatively greater fraction compared with that of the $\Sigma5$ boundary because the grain boundary energies of bcc metals are more sensitive to the grain boundary plane orientation than to the misorientation of the lattice. In the fcc metals, the $\Sigma3$ boundary is observed as pure twist boundaries. However, in the bcc metals, it appears as symmetric tilt boundaries. Conversely, in the bcc metals, the $\Sigma5$ boundary is observed as pure twist boundaries [24]. It has also been suggested that the distribution of the grain boundary normal undergoes significant change by the crystal lattice structure for a given misorientation angle, and that there exists a completely different set of low-energy grain boundary planes in the bcc lattice compared with the fcc crystal structure [25]. Based on these experimental results, the Nb tube that was caliber-rolled at the highest speed had the largest internal energy value owing to the high dislocation density materials. Hence, from the fraction of the $\Sigma3$ boundary that increased with the increase of the caliber-rolling speed, it is evident that the CSL boundaries with low-energy were primarily formed in the sample to reduce its energy. This is also supported by the fact that the coherent twin had the smallest boundary energy amongst the surveyed boundaries. However, the boundary was neither as small nor as uniquely small as that in the fcc metals [26].

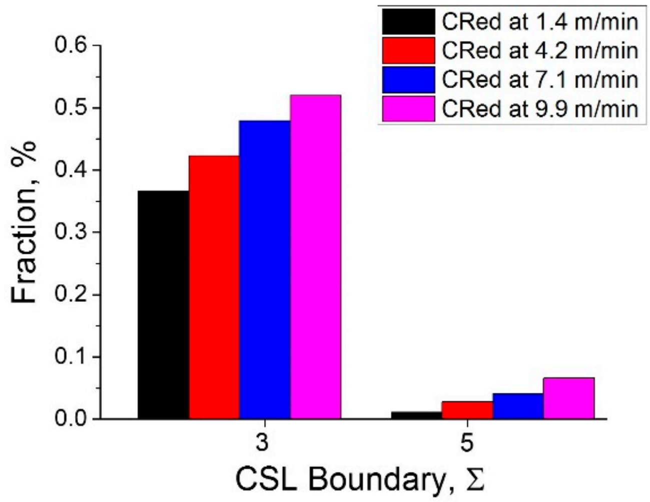

Figure 6. Comparison of fraction of CSL boundaries in Nb tubes caliber-rolled at highest and lowest speed.

5. Conclusions

In this study, Nb tubes mainly used as superconductivity materials were fabricated using the caliber-rolling process at various rolling-speeds from 1.4 to 9.9 m/min at ambient temperature. The effect of the caliber-rolling speed on the microstructure and microtexture of the Nb tubes was investigated based on the EBSD data. The following conclusions were drawn from this study:

(1) The microstructure of the Nb tube was refined and formed in grains with a higher fraction of low angle grain boundaries by applying the caliber-rolling process. However, the mean grain size of the caliber-rolled tubes was approximately identical, regardless of the caliber-rolling speed.

(2) The dislocation density of the Nb tube increased with the caliber-rolling speed at ambient temperature, according to the Orowan equation. This can only be explained in terms of the Peierls mechanism, and not in terms of the dislocation drag process caused by a low strain rate of less than 10^3 s^{-1}.

(3) By increasing the caliber-rolling speed, the fraction of the CSL boundaries with low energy increased, which contributed to retard the increasing rate of dislocation density. Then, the <112> fiber texture developed as the intensity of the entire texture weakened, and the <111> fiber texture disappeared. Based on the results, the productivity of the Nb tubes can be improved because the fraction of the CSL boundaries increases as a function of the caliber-rolling speed.

Author Contributions: Conceptualization, J.L., H.J.; methodology, J.L.; validation, J.L., H.J.; formal analysis, J.L.; investigation, J.L., H.J.; resources, J.L., H.J.; data curation, J.L.; writing—original draft preparation, J.L.; writing—review and editing, J.L.; supervision, H.J.; project administration, H.J.

Funding: This research was funded by a Grant from the Fundamental R&D Program (10053590) funded by the Ministry of Trade, Industry and Energy, Korea.

Conflicts of Interest: The authors declare no conflict of interest.

References

1. Li, Y.Z. Thermal properties of NbTi superconductor wire and its heat release performance over quench. *Mater. Sci. Eng. A* **2000**, *292*, 194–197. [CrossRef]
2. Echarri, A.; Spsdoni, M. Superconducting Nb_3Sn: A review. *Cryogenics* **1971**, *11*, 274–284. [CrossRef]

3. Willens, R.H.; Geballe, T.H.; Gossard, A.C.; Maita, J.P.; Menth, A.; Hull, G.W., Jr.; Soden, R.R. Superconductivity of Nb_3Al. *Solid State Commun.* **1969**, *7*, 837–841. [CrossRef]
4. Jie, H.; Qiu, W.; Billah, M.; Mustapic, M.; Patel, D.; Ma, Z.; Gajda, D.; Morawski, A.; Cetner, T.; Shahabuddin, M.; et al. Md Shahriar A Hossain, Superior transport *Jc* obtained in in-situ MgB_2 wires by tailoring the starting materials and using a combined cold high pressure densification and hot isostatic pressure treatment. *Scr. Mater.* **2017**, *129*, 79–83. [CrossRef]
5. Wang, X.; Li, J.; Jiang, Z.; Zhu, W.-L.; Shan, D.; Guo, B.; Cao, J. Size effects on flow stress behavior during electrically-assisted micro-tension in a magnesium alloy AZ31. *Mater. Sci. Eng. A* **2016**, *659*, 215–224. [CrossRef]
6. Wang, X.; Sánchez Egea, A.J.; Xu, J.; Meng, X.; Wang, Z.; Shan, D.; Guo, B.; Cao, J. Current-Induced Ductility Enhancement of a Magnesium Alloy AZ31 in Uniaxial Micro-Tension Below 373 K. *Materials* **2019**, *12*, 111. [CrossRef] [PubMed]
7. Zhang, X.; Li, H.; Zhan, M. Mechanism for the macro and micro behaviors of the Ni-based superalloy during electrically-assisted tension: Local Joule heating effect. *J. Alloys Compd.* **2018**, *742*, 480–489. [CrossRef]
8. Sánchez Egea, A.J.; González Rojas, H.A.; Celentano, D.J.; Peiró, J.J. Mechanical and metallurgical changes on 308L wires drawn by electropulses. *Mater. Des.* **2016**, *90*, 1159–1169. [CrossRef]
9. Doiphode, R.L.; Narayana Murty, S.V.S.; Prabhu, N.; Kashyap, B.P. Effects of caliber rolling on microstructure and room temperature tensile properties of Mg–3Al–1Zn alloy. *J. Magnes. Alloys* **2013**, *1*, 169–175. [CrossRef]
10. Taylor, G.I. The deformation of crystals of β-brass. *Proc. R. Soc. Lond. A* **1928**, *118*, 1–24. [CrossRef]
11. Christian, J.W. Some surprising features of the plastic deformation of body-centered cubic metals and alloys. *Metall. Trans. A* **1983**, *14*, 1237–1256. [CrossRef]
12. Hoge, K.G.; Mukherjee, A.K. The temperature and strain rate dependence of the flow stress of tantalum. *J. Mater. Sci.* **1977**, *12*, 1666–1672. [CrossRef]
13. Liu, J.; Morries, J.G. Texture and grain-boundary evolutions of continuous cast and direct chill cast AA 5052 aluminum alloy during cold rolling. *Metall. Mater. Trans. A* **2003**, *34*, 951–966. [CrossRef]
14. Takayama, Y.; Szpunar, J.A. Stored Energy and Taylor Factor Relation in an Al-Mg-Mn Alloy Sheet Worked by Continuous Cyclic Bending. *Mater. Trans.* **2004**, *45*, 2316–2325. [CrossRef]
15. Hou, J.; Peng, Q.J.; Lu, Z.P.; Shoji, T.; Wang, J.Q.; Han, E.-H.; Ke, W. Effects of cold working degrees on grain boundary characters and strain concentration at grain boundaries in Alloy 600. *Corros. Sci.* **2001**, *53*, 1137–1142. [CrossRef]
16. Dutta, R.K.; Petrov, R.H.; Delhez, R.; Hermans, M.J.M.; Richardson, I.M.; Bottger, A.J. The effect of tensile deformation by in situ ultrasonic treatment on the microstructure of low-carbon steel. *Acta Mater.* **2013**, *61*, 1592–1602. [CrossRef]
17. Liu, Q.; Jensen, D.J.; Hansen, N. Effect of grain orientation on deformation structure in cold-rolled polycrystalline aluminium. *Acta Mater.* **1998**, *46*, 5819–5838. [CrossRef]
18. Kobayashi, M.; Takayama, Y.; Kato, H. Preferential Growth of Cube-Oriented Grains in Partially Annealed and Additionally Rolled Aluminum Foils for Capacitors. *Mater. Trans.* **2004**, *45*, 3247–3255. [CrossRef]
19. Florando, J.N.; El-Dasher, B.S.; Chen, C. Effect of strain rate and dislocation density on the twinning behavior in tantalum. *AIP Adv.* **2016**, *6*, 04520. [CrossRef]
20. Lau, S.S.; Ranji, S.; Mukherjee, A.K.; Thomas, G.; Dorn, J.E. Dislocation mechanisms in single crystals of tantalum and molybdenum at low temperatures. *Acta Metall.* **1967**, *15*, 237–244. [CrossRef]
21. Cottrell, A.H.; Bilby, B.A. A mechanism for the growth of deformation twins in crystals. *Philos. Mag.* **1951**, *42*, 573–581. [CrossRef]
22. Sleeswyk, A.W. Perfect dislocation pole models for twinning in the f.c.c. and b.c.c. lattices. *Philos. Mag.* **1974**, *29*, 407–421. [CrossRef]
23. Randle, V.; Rohrer, G.S.; Miller, H.M.; Coleman, M.; Owen, G.T. Five-parameter grain boundary distribution of commercially grain boundary engineered nickel and copper. *Acta Mater.* **2008**, *56*, 2363–2373. [CrossRef]
24. Beladi, H.; Rohrer, G.S. The Distribution of Grain Boundary Planes in Interstitial Free Steel. *Metall. Mater. Trans. A* **2013**, *44*, 115–124. [CrossRef]

25. Wolf, D.; Phillpot, S. Role of the densest lattice planes in the stability of crystalline interfaces: A computer simulation study. *Mater. Sci. Eng. A* **1989**, *107*, 3–14. [CrossRef]
26. Ratanaphan, S.; Oimsted, D.L.; Bulatov, V.V.; Holm, E.A.; Rollett, A.D.; Rohrer, G.S. Grain boundary energies in body-centered cubic metals. *Acta Mater.* **2015**, *88*, 346–354. [CrossRef]